Anisotropic Electron Transport Limits Performance in Bi$_2$WO$_6$ Photoanodes

Benjamin Moss,[a]* Haonan Le,[a] Sacha Corby,[a] Kazuki Morita,[b] Shababa Selim,[a] Carlos Sotelo-Vazquez,[c] Yunuo Chen,[a] Alexander Borthwick,[a] Anna Wilson,[a] Chris Blackman,[c] James R. Durrant,[a] Aron Walsh[b,d] and Andreas Kafizas,[a,e]*

[a]*Department of Chemistry, Molecular Science Research Hub, Imperial College London, White City Campus, London, W12 0BZ, U.K.*

[b]*Department of Materials, Imperial College London, Exhibition Road, London SW7 2AZ, U.K.*

[c]*Department of Chemistry, University College London, 20 Gordon Street, London, WC1H 0AJ, U.K.*

[d]*Department of Materials Science and Engineering, Yonsei University, Seoul 03722, South Korea*

[e]*Grantham Institute for Climate Change, Imperial College London, South Kensington, London, SW7 2AZ, U.K.*

corresponding authors: b.moss14@imperial.ac.uk and a.kafizas@imperial.ac.uk

Abstract

Bi$_2$WO$_6$ is one of the simplest members of the versatile Aurivillius oxide family of materials. An intriguing model system for Aurivillius oxides, BiVO$_4$ exhibits low water oxidation onset potentials (~0.5-0.6 V$_{RHE}$) for driven solar water oxidation. Despite this, Bi$_2$WO$_6$ also produces low photocurrents in comparison to other metal oxides. Due to a lack of *in-situ* studies, the reasons for such poor performance are not understood. In this study, Bi$_2$WO$_6$ photoanodes are synthesised by aerosol-assisted chemical vapour deposition. The charge carrier dynamics of Bi$_2$WO$_6$ are studied *in-situ* under water oxidation conditions and the rate of both bulk recombination and water oxidation is found to be comparable to other metal oxide photoanodes. However, the rate of electron extraction is at least 10 times slower than slowest kinetics previously reported in an oxide photoanode. First-principles analysis indicates that the slow electron extraction kinetics are linked to a strong anisotropy in the conduction band. Preferred or epitaxial growth along the conductive axes is a strategy to overcome slow electron transport and low photocurrent densities in layered materials such as Bi$_2$WO$_6$.

Introduction

To mitigate climate change,[1,2] there is a growing need to develop low cost renewable routes to hydrogen fuel.[3,4] One of the most promising routes to renewable hydrogen is to harness solar energy to convert water into hydrogen and oxygen using photoelectrochemical cells.[5–7] Metal oxides are attractive photoelectrodes as they often show high durability and are typically cheap to produce at scale.[8] To date the application of oxide based photoelectrochemical water splitting technologies is limited by a dearth of materials with narrow enough band gaps to effectively harvest the solar spectrum and optoelectronic properties which lend themselves to high efficiencies.[9] The search for efficient, low cost metal oxides with improved visible light harvesting characteristics has resulted in an expanding library of ternary and quaternary metal oxides, some of which show promise as photoanodes for the rate limiting water oxidation half-reaction.[10,11] An unexplored and potentially versatile group of ternary/quaternary oxides is the family of Aurivillius oxides: $(Bi_2O_2)^{2+}(A_{m-1}B_mO_{3m+1})^{2-}$.

The layered structure of these materials implies a vast library of possible sub-phases, each with a distinct set of optoelectronic properties, whilst studies of B site substitution demonstrate the possibility of band gap engineering to enhance solar harvesting.[12,13] Preliminary studies indicate that some members show promise in photocatalytic and photoelectrochemical applications.[14–16] However, relatively little is known about the factors which govern water oxidation efficiency in even the simplest examples of this diverse and complex family of materials.

Bi_2WO_6 is one of the simplest members of the Aurivillius oxide family,[17] and possesses a layered structure with alternating $(Bi_2O_2)^{2+}$ and octahedral $(WO_4)^{2-}$ layers, forming an orthorhombic unit cell (Fig. 1a).[18] Bi_2WO_6 exhibits a ~2.7 – 2.8 eV band gap,[19] corresponding to a maximum theoretical solar-to-hydrogen efficiency of ~5%.[20] Solar water splitting using Bi_2WO_6 was first demonstrated by Kudo *et al*.[21] It has since been shown that Bi_2WO_6 is an n-type semiconductor[22] capable of photoelectrochemically oxidising water.[23–27] Bi_2WO_6 photoanodes typically show early onset potentials (~0.5 V_{RHE}), but to date, have exhibited low photocurrents.[26,27] Various strategies have been pursued in an effort to improve the photocatalytic activity of Bi_2WO_6, which include the use of surface co-catalysts,[26,28] doping,[29–33] and forming heterojunctions.[34–38] However, in order to improve the performance of Bi_2WO_6 through rational design, a better understanding of its intrinsic charge carrier behaviour is required.[39] To date, there have only been a handful of such studies on Bi_2WO_6.[16,40–44] Herein, we carry out the first study of charge carrier dynamics during water oxidation. We determine timescales of bulk recombination, charge separation, water oxidation and electron extraction in Bi_2WO_6, comparing these to other well-known metal oxides. Electron extraction was found to be 10 times slower than the slowest extraction rate previously reported for an oxide photoanode.[45] Using density functional theory, we link poor electron transport properties to a spatial anisotropy of the conduction band, which is localised in (001) planes within the material. This leads to new insight into potential design strategies to overcome poor photocurrent in Bi_2WO_6 and other oxide photoelectrodes exhibiting similar layered crystal structures.

Methods

Bi_2WO_6 coatings were grown on FTO glass substrates (TEK 15; 2.5 × 2.7 cm) using an aerosol-assisted chemical vapour deposition (AACVD) method, in a cold wall reactor. Substrates were heated from underneath using a graphite heating block. The inlet to the reactor was equipped with a cooling water jacket to prevent any prior decomposition of the precursor before reaching the reactor. The precursor solution contained triphenyl bismuth (0.195 g, 22 mM) and tungsten hexacarbonyl (0.0388 g, 5.5 mM) in an acetone: methanol mixture (2:1; 20 ml). The solution was sonicated for 10 min to dissolve the precursors (VWR ultrasonic cleaner, 30 W, 45 kHz). The solution was then aerosolized using an ultrasonic humidifier (2 MHz, Liquifog, Johnson Matthey) and carried over the heated FTO substrate (375 °C) using an inert N_2 carrier gas (99.99%, BOC) at a flow rate of 300 sccm (MFC, Brooks) over a period of ~20 min, until the solution had been fully transferred. The coatings formed were subsequently annealed at 550 °C in air for 6 hrs.

Powder X-ray diffraction (PXRD) was conducted using a Bruker Lynx-Eye X-ray diffractometer equipped with a monochromated Cu-K_α (1.5406 Å) X-ray source, and compared with standards from the Physical Sciences Data-Science (PSDS) database.[46] Raman spectra were obtained using a Horiba LabRam Infinity equipped a helium-neon laser (633 nm, 25 mW). The system was calibrated to a silicon reference, and samples were analysed over the 200 – 1000 cm^{-1} range. Standards were acquired from RRUFF project database.[47] For scanning electron microscopy (SEM), 10 nm of chromium was deposited on samples by sputtering to prevent charging. Images were taken using a LEO GEMINI 1525 microscope using a 1.5 keV electron beam. EDX was performed on the same instrument using an Oxford Instruments X-act detector at a beam voltage of 20 keV. High-resolution transmission electron microscopy (HR-TEM)

images were obtained using a high-resolution TEM Jeol 2100 with a LaB_6 electron source operating at an acceleration voltage of 200 kV. Micrographs were recorded on a Gatan Orius charge-coupled device (CCD). Bi_2WO_6 particles were removed from coatings using a spatula, suspended in n-hexane, sonicated, and then drop-casted onto a 400 Cu mesh lacy carbon grid (Agar Scientific Ltd.) for analysis. X-ray photoelectron spectroscopy (XPS) was performed using a Thermo Scientific™ K-Alpha™ instrument. The instrument uses monochromated and micro-focused Al-K_α (hv = 1486.6 eV) radiation to eject photoelectrons. These were then analysed using a 180° double-focusing hemispherical analyser with a 2D detector. A flood gun was used to minimize sample charging. Spectra were collected at 2 x 10^{-9} mbar base pressure. All samples were referenced to the C-C peak of adventitious carbon in the C 1s spectrum at a binding energy of 284.8 eV to correct for any charge that is not neutralised by the flood gun. Data was analysed using CASAXPS software.[48] Ultra-violet visible (UV-Vis) transmission spectroscopy was performed on a Shimadzu UV-vis 2600 spectrophotometer equipped with an integrating sphere.

All photoelectrochemical analyses were carried out in a homemade PEEK cell with quartz windows. Analyses were typically carried out in 0.1 M phosphate buffer (0.05 M K_2HPO4, 0.05 M KH_2PO4; pH = 7) in Milli-Q-water (Millipore Corp., 18.2 MΩ·cm at 25 °C), with the exception of our hole scavenger studies, which were carried out in 0.1 M sodium sulphite (pH = 6) and compared with measurements carried out in 0.1 M sodium sulphate (pH = 7). For all measurements, a three-electrode configuration was used, with a Pt mesh counter electrode, an Ag/AgCl reference electrode in sat. $KCl_{(aq)}$ (0.197 V_{NHE} at 25 °C; Metrohm), and a Bi_2WO_4 photoanode placed at the working electrode. An Autolab potentiostat (PGSTAT12 with an FRA2 module) was used to apply voltage and measure currents. All applied voltages are reported *vs* the reversible hydrogen electrode (V_{RHE}), converted using the Nernst equation.

$$V_{RHE} = V_{Ag/AgCl} + (0.0591 \times \text{pH}) + V_{Ag/AgCl}^{\emptyset} \qquad \text{(Eq 1)}$$

where $V_{Ag/AgCl}$ is the applied potential *vs* the reference electrode and $V_{Ag/AgCl}^{\emptyset}$ is the standard potential of the reference electrode.

For measuring (photo)current–voltage curves, a 365 nm LED light source was used (LZ1-10U600, LedEngin. Inc.) to photoexcite the photoanode. Light intensity was measured using an optical power meter (PM 100, Thorlabs) coupled with a power sensor (S120UV, Thorlabs). For measuring the incident photon to current efficiency (IPCE) an ozone-free xenon lamp (75 W, Hamamatsu) was coupled to a monochromator (OBB-2001, Photon Technology International). The IPCE was calculated using the following equation:

$$IPCE(\%) = (I_{ph} \times 1239.8)/(P_{mono} \times \lambda) \times 100 \qquad \text{(Eq 2)}$$

where I_{ph} is the photocurrent (mA.cm^{-2}), 1239.8 is the multiplication of Planck's constant with the speed of light (eV.nm), P_{mono} is the light power at a given wavelength (mW.cm^{-2}) and λ is the wavelength of the monochromated light (nm).

Ultrafast Transient Absorption Spectroscopy (uf-TAS), from the femtosecond to nanosecond timescale, was measured in transmission mode using a regeneratively amplified Ti:sapphire laser system (Solstice, Spectra-Physics) and Helios spectrometers (Ultrafast Systems), which generates 800 nm laser pulses (92 fs pulse width, 1 kHz repetition rate). To generate the pump, a fraction of the 800 nm beam was directed through a sequence of optical parametric amplifier (TOPAS Prime, Spectra-Physics) and a frequency mixer (NIR/UV-Vis, Light Conversion) to tune the excitation wavelength to 355 nm. The intensity of the pump was modulated using neutral density filters, and measured using

an energy meter (VEGA, P/N 7Z01560, OPHIR Photonics), fitted with a 0.5 mm diameter aperture. The pump beam at the sample was ≥0.5 mm. A visible white light continuum (WLC) was used as the probe, generated from a fraction of the 800 nm pulse, focused onto a Ti:sapphire crystal. The probe beam was delayed with respect to the pump beam using a motorised delay stage to alter the path length of the probe beam before generation of the WLC. To reduce the noise, the WLC was split into two beams, one of which is passed through the sample, and the other used as a reference. Both beams were subsequently focused onto separate fibre-optic coupled, multichannel spectrometers (CMOS sensors). Alternate pump pulses were blocked using a synchronised chopper (500 Hz). As such, absorption spectra of the excited and unexcited sample were obtained to determine the time-resolved absorption difference spectrum. Time zero was then adjusted to match the rise of the signal at each wavelength. The presented decay kinetics were averaged over a spectral range of *ca.* 10 nm. Measurements were carried out in air.

Slower timescale transient absorption spectroscopy from the microsecond to second timescale, was measured in transmission mode. A Nd:YAG laser (OPOTEK Opolette 355 II, ~6 ns pulse width) was used as the excitation source, generating 355 nm UV light from the third harmonic (~1.5 mJ.cm^{-2} per pulse, repetition rate of 0.65 Hz). The probe light was a 100 W Bentham IL1 quartz halogen lamp. Long pass filters (Comar Instruments) were placed between the lamp and sample to minimize short wavelength irradiation of the sample. Transient changes in absorption/diffuse reflectance from the sample was collected by a 2" diameter, 2" focal length lens and relayed to a monochromator (Oriel Cornerstone 130) and measured at select wavelengths between 500 and 1100 nm. Time-resolved changes in light transmission were collected using a Si photodiode (Hamamatsu S3071). Data at times faster than 3.6 ms was recorded by an oscilloscope (Tektronics DPO3012) after passing through an amplifier box (Costronics), whereas data slower than 3.6 ms was recorded on a National Instrument DAQ card (NI USB-6251). Each kinetic trace was obtained from the average of between 100 and 250 laser pulses. Acquisitions were triggered by a photodiode (Thorlabs DET10A) exposed to laser scatter. Data was acquired and processed using home-built software written in Labview. Measurements were carried out *in situ* in 0.1 M phosphate buffer within our homemade PEEK cell in a three-electrode configuration. The voltage was applied using an Autolab potentiostat (PGSTAT 101, Metrohm). Transient photocurrents (TPC) were measured simultaneously by the oscilloscope.

Plane-wave density functional theory (DFT) calculations were performed using VASP[49–51], and the atomic structures were visualised using the VESTA package.[52] The geometry optimisation[49] was performed with PBEsol exchange correlation functional on a primitive cell consisted of 36 atoms, while the density of states and the band structures were calculated with HSE06 exchange correlation functional. *k*-point sampling of 5 × 5 × 2, plane-wave cut-off of 550 eV, and convergence criteria of 10^{-}
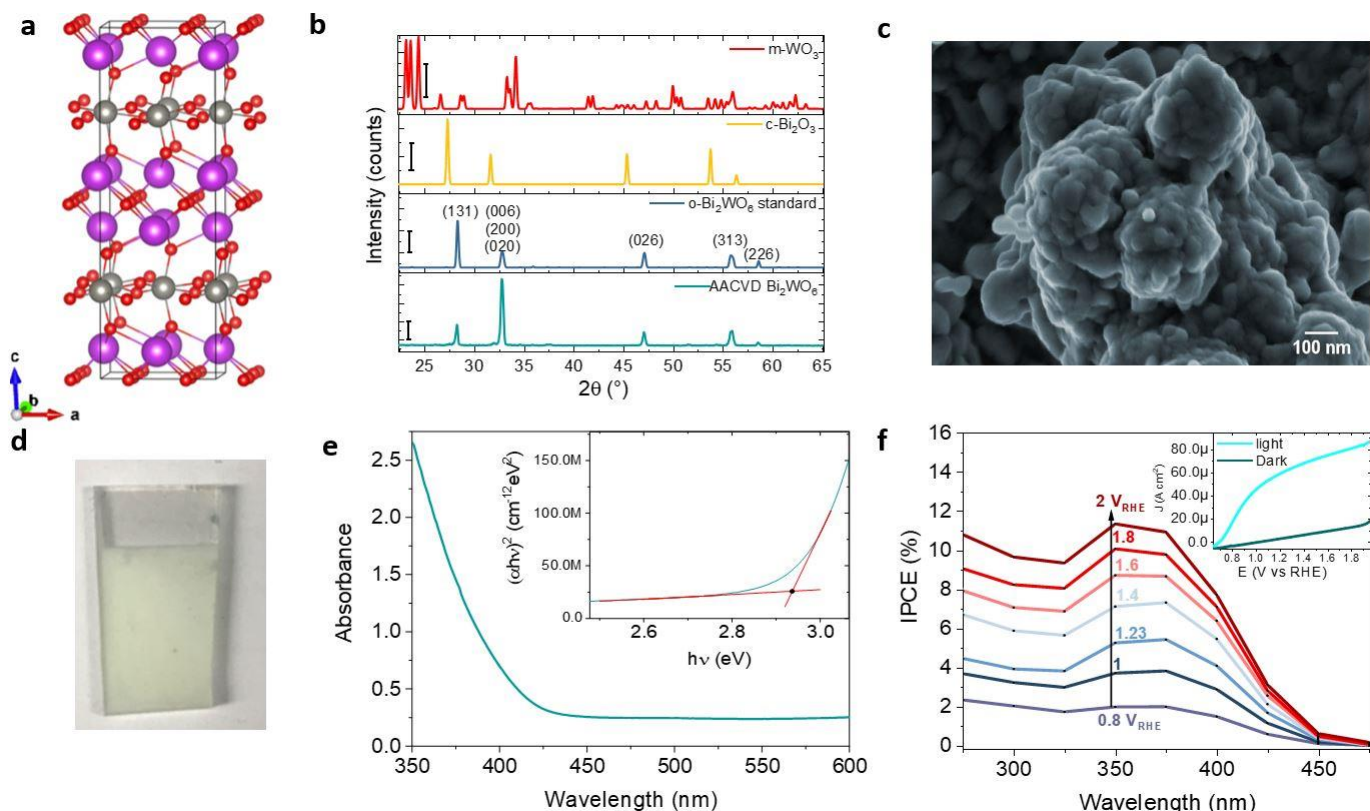
Figure 1: (a) Orthorhombic unit cell of Bi_2WO_6. Red, purple and grey spheres correspond to oxygen, bismuth and tungsten respectively. XRD patterns of the AACVD Bi_2WO_6 shown alongside known standards for orthorhombic (o) Bi_2WO_6,[54] cubic (c) Bi_2O_3[50] and monoclinic (m) WO_3[51]. Scale bar: 300 counts. (c) SEM image of AACVD Bi_2WO_6 showing micron sized mounds composed of smaller crystallites. (d) Photograph of AACVD Bi_2WO_6 film (e) Absorbance spectrum of AACVD Bi_2WO_6 with inset showing a direct bandgap of 2.93 eV. (f) IPCE spectrum of AACVD Bi_2WO_6 at various applied potentials. Inset: linear sweep voltammograms (10 mV s^{-1}) in the dark and under simulated solar irradiation. Electrochemical measurements performed using front irradiation with phosphate buffer (pH 7) and a three-electrode configuration.

^{8} eV were employed. The optimised crystal structure has been uploaded to an open repository at https://github.com/WMD-group/Crystal_structures.

Results and discussion

Bi_2WO_6 films were grown on FTO glass substrates using an aerosol assisted chemical vapour deposition (AACVD) method and a previously reported setup (See Methods for details).[53] X-ray diffraction (XRD) of the resulting film is shown in Figure 1b. Phase pure orthorhombic Bi_2WO_6 ($P2_1ab$; a = 5.4559 Å, b =5.4360 Å, c = 16.4297 Å, $\alpha = \beta = \gamma = 90°$)[54] is observed with preferred growth of (006), (200) and (020) planes. Scherrer line broadening analysis[55] showed that the average crystallite diameter in the Bi_2WO_6 coating was ~50 nm. A LeBail refinement of our XRD data against a crystallographic standard (Fig. S0a) indicates that differences in between the measured pattern and the standard can be attributed to preferred growth. This is consistent with a more detailed comparison of the measured pattern against standards for WO_3 and Bi_2O_3 (S0b), where the absence of peaks at 24.4° and 45.35° (S0c, d) indicate that any impurity phases are found in concentrations beneath the detection limit of the diffractometer. Purity is further corroborated by X-ray photoelectron spectroscopy (Fig. S1) which indicates the film is primarily composed of W^{6+}, Bi^{3+} and O^{2-} states with a Bi: W: O ratio of 2.0: 0.74:

5.3, which is close to the expected stoichiometric ratio (See Figure S1 for a detailed discussion of oxidation states).

High-resolution scanning electron microscopy (SEM) images of the AACVD Bi_2WO_6 films are shown in Figure 1c. The coatings are composed of rough, micron-sized mounds, themselves composed of smaller (< 100 nm diameter) particles. Cross-sectional SEM (Fig. S2) reveals the films to be, on average, ~1.5 μm thick, with good film coverage and few pinholes. EDX analysis (Fig. S3) indicates that the Bi_2WO_6 coatings contained Bi, W and O. However, some nanoscale regions of high W content and low Bi content were observed (Fig. S3). These are attributed to WO_3 impurity crystal growth at concentrations below the resolution of XRD (roughly ≤ 1%). Due to the low concentration of WO_3 and the distinct behaviour of the Bi_2WO_6 films studied herein from AACVD WO_3 films made previously in our group,[45] we do not consider this minor impurity to be a significant factor influencing the behaviour of the films. High magnification SEM images (Fig. S4) images reveal that the micron-sized mounds of the coating are themselves composed of interconnected nanoparticles ranging in diameter from ~20-100 nm, consistent with the results of Scherrer analysis.

The optical characteristics of the AACVD Bi_2WO_6 films are evaluated in Figure 1d and 1e, which respectively show a photograph of a typical film and the corresponding optical absorbance spectrum. Films were opaque with a slight yellow colour. This is reflected in the absorbance spectrum, which shows an absorbance onset around 425 nm superimposed on a flat background of 0.25 a.u. induced by strong scattering (Fig. S5). Consistent with the absorbance onset, a direct allowed bandgap of 2.93 eV was measured using the Tauc method, similar to previous literature findings.[25,37]

We assessed the performance of the AACVD Bi_2WO_6 as photoanodes for the photoelectrochemical oxidation of water. Incident photon to current efficiency (IPCE) spectra at various applied potentials are shown in Figure 1f. A maximum IPCE of 4% was observed with 375 nm light at 1.23 V_{RHE}, with a roughly linear dependence of efficiency on applied potential. A distinct wavelength dependence is also observed, with IPCE increasing with decreasing wavelength until 350-375 nm, presumably due to increased photon absorption, after which a decrease is observed. A typical current-voltage curve is shown in the inset of Figure 1f. Here, the onset of photoelectrochemical water oxidation is observed at 0.6 V_{RHE} with a photocurrent at 1.23 V_{RHE} of ~0.06 mA cm^{-2}. The photoelectrochemical stability of our Bi_2WO_6 photoanodes was measured at 1.23 V_{RHE} under chopped, intense 375 nm irradiation (Fig. S6). Within a few minutes, the photocurrent dropped from ~3.2 to ~2.8 mA cm^{-2}. However, after this initial drop (equivalent to an ~19% loss in performance), the photocurrent remained approximately constant for the 15-hour testing period (see Fig. S6 for further discussion).

The performance of the AACVD Bi_2WO_6 coatings studied herein agree well with the literature trend of relatively early onset potentials but poor photocurrent density (see Table S1 for a comparison). To further understand the origin of low photocurrent densities relative to other similar materials, we turned to transient absorption spectroscopy (TAS) combined with simultaneous transient charge extraction measurements; comparing these results to other metal oxides known to exhibit higher photocurrents such as TiO_2, WO_3 and $BiVO_4$.

To better understand the influence of recombination on the photocurrent produced by Bi_2WO_6, we performed ultra-fast (fs-ns) and slow (μs-s) TAS under an inert atmosphere. Here, charges are not separated by a depletion layer and can only recombine. The rates of recombination in the absence of a space charge layer (hereafter 'bulk' recombination) can vary by orders of magnitude between different metal oxides on ultra-fast timescales, which in turn can impact efficiency. For example, the $t_{50\%}$ of transient photogenerated charge in Fe_2O_3 under an inert atmosphere ranges from 10-30 ps, whilst transients for TiO_2 measured under the same conditions have a $t_{50\%}$ of 1000-2000 ps.[56] Figure
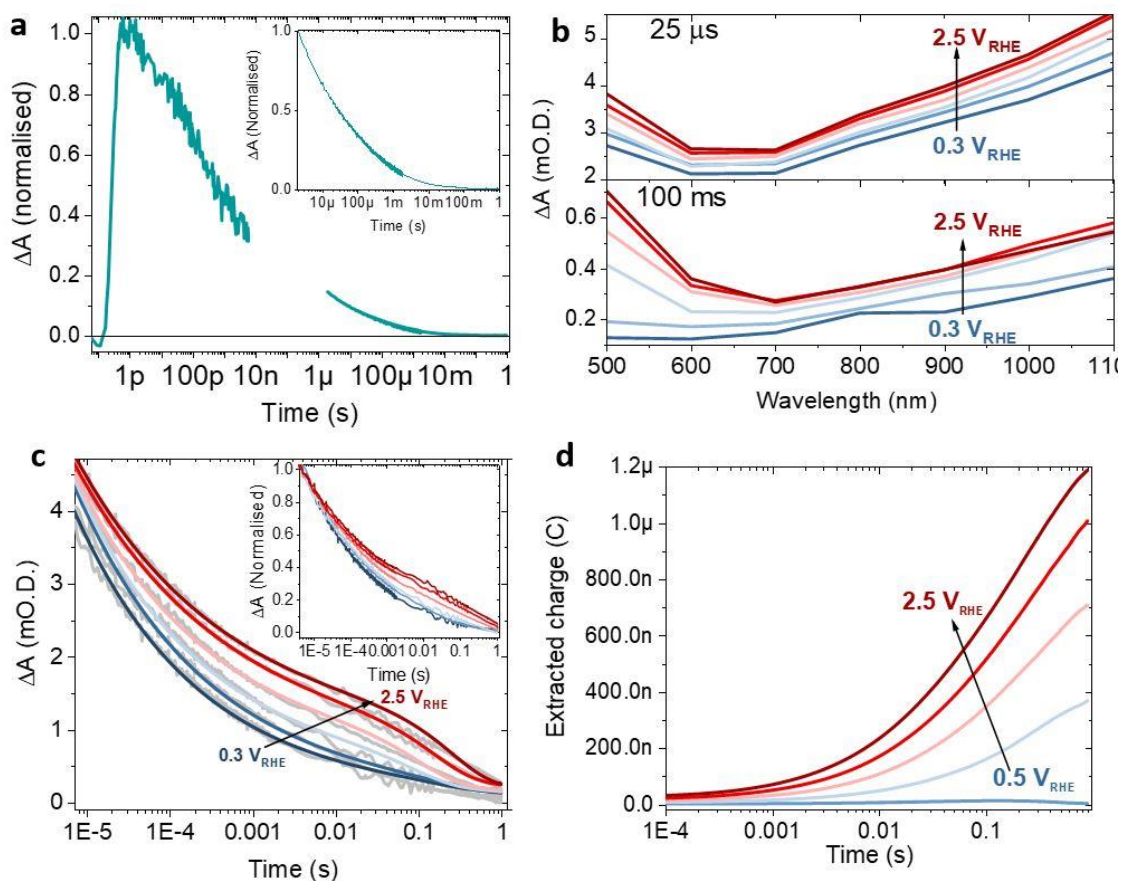
Figure 2: (a) Normalised transient recombination kinetics from the ps-s timescales, measured at 650 nm under an inert atmosphere. Inset shows normalised recombination kinetics from μs to s. (b) Transient spectra of AACVD-Bi$_2$WO$_6$ at 25 μs and 250 ms at 0.3, 0.5, 1, 1.5, 2 and 2.5 V$_{RHE}$. (c) Transient kinetics measured at 500 nm at 0.3, 0.5, 1, 1.5, 2 and 2.5 V$_{RHE}$. Experimental data is shown in grey, the results of fitting to the sum of a power law function plus an exponential function are shown in colour. Inset: TA kinetics normalised at 5 μs. (d) Time resolved charge extraction measured during TA experiments, showing 50% charge extraction times of ~100 ms. Conditions for b-d: front irradiation using phosphate buffer (pH 7) and a three-electrode configuration.

2a shows bulk TA recombination kinetics of Bi$_2$WO$_6$ from fs to s. Electron-hole recombination was investigated by probing at 650 nm following excitation with a 355 nm laser flash. A relatively slow decaying transient is observed, with a t$_{50\%}$ decay of ~0.20 ns from 2 ps was observed, which decays more slowly at lower excitation densities, indicative of bimolecular type recombination (*i.e.* nongeminate electron/hole recombination, see Fig. S7 for intensity dependence).[57] This is faster than anatase TiO$_2$ on ultrafast timescales[56,58] but slower than Fe$_2$O$_3$, BiVO$_4$ or WO$_3$.[56,59] On slower timescales, power law (ΔOD ∝ t$^{-\alpha}$ where α≈0.26) recombination dynamics were observed. Power law decays occur in a broad range of metal oxides, arising when ideal 'bimolecular' electron/hole recombination (α = 1) is disrupted by a multiple trapping process, in which a carrier must be repeatedly thermally excited in order to move, and ultimately recombine.[57,60] Here, a t$_{50\%}$ of around 100 μs is observed from 1 μs, commensurate to slow timescale bulk recombination in WO$_3$ (10-100 μs, see Table S2 and Fig. S8 for comparison to literature) .

To interrogate the role of recombination in the presence of a charge separating depletion layer[61,62] in limiting photocurrent, the TA kinetics of AACVD Bi$_2$WO$_6$ photoanodes, was monitored *in-situ* under water oxidation conditions. Figure 2b shows the TA spectrum at 25 μs (upper panel) and 250 ms (lower

panel) after front irradiation with a 1.2 mJ cm^{-2} laser pulse at various applied potentials (0.3 to 2.5 V$_{RHE}$). A strong increase in amplitude at 250 ms is observed in the blue (λ_{max} ~500 nm) relative to longer wavelengths as the potential is increased. This effect has previously been observed in TiO$_2$,[63] BiVO$_4$[61] and Fe$_2$O$_3$[56] photoanodes, and is attributed to improved charge separation arising from the growth of a depletion layer with increasing potential. As such, we attribute the increased signal observed at ~500 nm to persistent, surface separated holes at the Bi$_2$WO$_6$ surface. This effect is clearly visible in the transient kinetics at 500 nm (Figure 2c). Here, a component exhibiting power law decay kinetics is observed at low applied potentials (0.3 and 0.5 V$_{RHE}$). As the t$_{50\%}$ of this decay is around 100 μs – similar to that observed under an inert atmosphere (Figure 2a) – we assign this decay component to bulk recombination occurring outside the space charge layer. As the potential is increased, a second, more persistent component in the TA emerges at later times (attributed to separation of charge in the depletion layer) which then decays exponentially. Fitting these decays with the sum of a power law and an exponential decay function reveals that persistent, exponentially decaying holes at potentials ≥1 V$_{RHE}$ decay with an approximate rate constant of approximately 7 s^{-1} (see Fig. S9 for details/fitting parameters). For potentials exceeding 1 V$_{RHE}$, the transient charge extracted during the experiment (Figure 2d) does not decrease at late times. A decrease would indicate the back recombination of separated surface holes with bulk electron, rather than reaction.[61,62] As this is not present, we assign this time constant to the reaction of holes with water.[61,62] The observed rate constant of *ca.* 7 s^{-1} is commensurate that observed in TiO$_2$ (~2 - 5 s^{-1}),[63] faster than Fe$_2$O$_3$ (0.7 s^{-1})[64] and BiVO$_4$ (1.3 s^{-1}),[61] but significantly slower than WO$_3$ (~2000 s^{-1}).[45] As with other metal oxides[61] the amplitude of this long lived exponential decay phase correlates with photocurrent, providing further indication that this decay arises from the reaction of photogenerated holes with water (S10).

Transient electron extraction kinetics, measured simultaneously during TA experiments, are shown in Figure 2d. Remarkably slow extraction kinetics are observed, differing by orders of magnitude from other metal oxides studied using the same technique. For example, even at the strongest potential studied herein, 50 % electron extraction times are around 100 ms. This is at least 10 times slower than the slowest extraction times previously observed in a metal oxide (WO$_3$ ~10 ms).[45] Further, in WO$_3$ photogenerated electrons travelled twice as far (*ca.* 3.6 μm thick film) to reach the external circuit than the AACVD Bi$_2$WO$_6$ studied herein (*ca.* 1.5 μm thick film), yet did so ten times faster. Other oxides, such as Fe$_2$O$_3$ and BiVO$_4$ show 50% extraction times around two orders of magnitude faster than AACVD Bi$_2$WO$_6$ (*ca.* 1ms).[20,59]

To understand the origin of the remarkably slow electron extraction, we turned to density functional theory (DFT) using the HSE06 functional to precisely calculate band structure (see Methods for details). Figure 3a shows the normalised total and partial density of states for Bi$_2$WO$_6$. The valence band (VB) maximum projects on to both Bi 6s and O 2p states. This coupling of Bi 6s and O 2p orbitals leads to an upward dispersion of the VB and a narrower band gap than would otherwise be expected.[65] Consistent with the results of a previous theoretical study screening Aurivillius oxides,[13] the conduction band (CB) minimum projects predominantly on W 5d states with some O 2p density. The CB exhibits a strong spatial anisotropy, illustrated by the iso-surface shown in Figure 3b. Here, the CB is confined to (WO$_4$$^{2-}$)$_n$ planes. The impact on the band structure is evident (Fig. 3c) as strong CB dispersion is observed along <100> (Γ to X) and <010> (Γ to Y) directions. In contrast, negligible dispersion is observed along <001> (Γ to Z), corresponding to out of plane interaction between WO$_4$$^{2-}$ units. Anisotropy in the band dispersion (effective masses) is compounded by the fact that on the ms-s timescale electron transport occurs through thermally activated polaron hopping.[45] Here, the probability of hopping (tunnelling) decays exponentially with distance, meaning that hopping from one (WO$_4$$^{2-}$) subunit to another across a larger (Bi$_2$O$_2$$^{2+}$)$_n$ plane will be slower than hopping between (WO$_4$$^{2-}$) subunits within a plane. This is consistent with the observation that electron extraction is ten

times slower in Bi_2WO_6 than in WO_3, where the connectivity is more isotropic. The same anistropic conduction does not occur for holes, as the O 2p based valence band is not confined to a given plane (Fig. 3c).
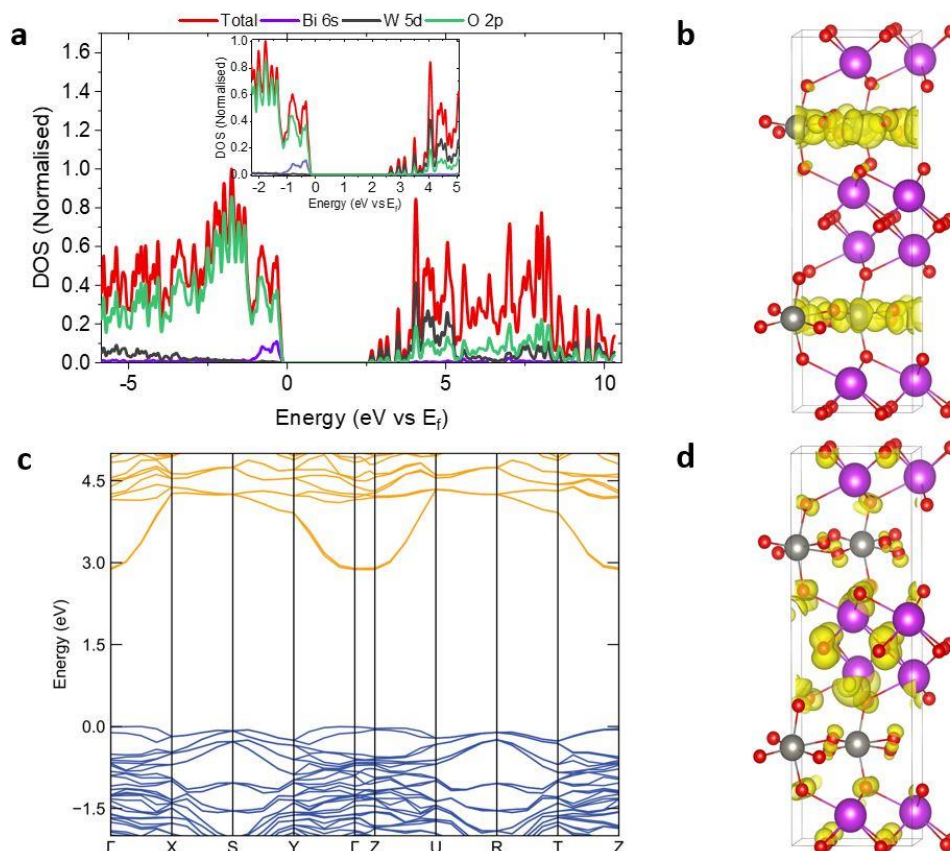

Figure 3: (a) Normalised total and partial density of states of Bi_2WO_6 (DFT-HSE06) with inset showing the region around the valence band maximum and conduction band minimum. (b) 0.003 e/$Å^3$ iso-surface for the conduction band of Bi_2WO_6. (c) band structure for Bi_2WO_6 showing strong in plane conduction band dispersion between Γ and X or Γ and Y but weak out of plane dispersion between Γ and Z. (d) 0.003 e/$Å^3$ iso-surface for the valence band of Bi_2WO_6.

To understand the impact of anisotropic electron transport in the AACVD Bi_2WO_6 films studied herein we return to our XRD data (Figure 1b). From simple inspection of the data, it is apparent that growing Bi_2WO_6 by AACVD leads to preferred growth in the randomly oriented crystallites that make up the micron size mounds in the film. By performing a LeBail refinement of our XRD data (Fig.1b) against a crystallographic standard (o-Bi_2WO_6 in Fig. 1b) the relative concentrations of different planes in AACVD Bi_2WO_6 can be quantified and compared to a crystallographic standard (Fig. S11). This analysis reveals that Miller planes in the (131) direction (2θ = 28.3°) grow less, whereas the Miller planes in the (006), (200) and (020) direction (2θ = 32.603°, 32.809° and 32.925° respectively) are enhanced. Figure 4a shows a simplified schematic of the orthorhombic unit cell of Bi_2WO_6 and illustrates the connection between different modes of preferred growth and electron transport. Hypothetically, very strong preferred growth of (h,0,0) or (0,k,0) planes would result in nano-rods with conduction band planes growing along the length of the rod. Strong preferred (h,k,0) growth would lead to sheets with similarly favourable conduction. However, stacking of (0,0,l) planes would lead to growth orthogonal to the favourable directions of electron transport. Figure 4b shows the result of categorising growth planes into three categories: growth planes along which CB electrons would exhibit a mobility in the presence of an electric field and are thus more conductive (*i.e.* (h,0,0), (0,k,0) or (h,k,0)); low mobility, poorly conducting (0,0,l) growth planes, and planes in which growth in favourable and unfavourable
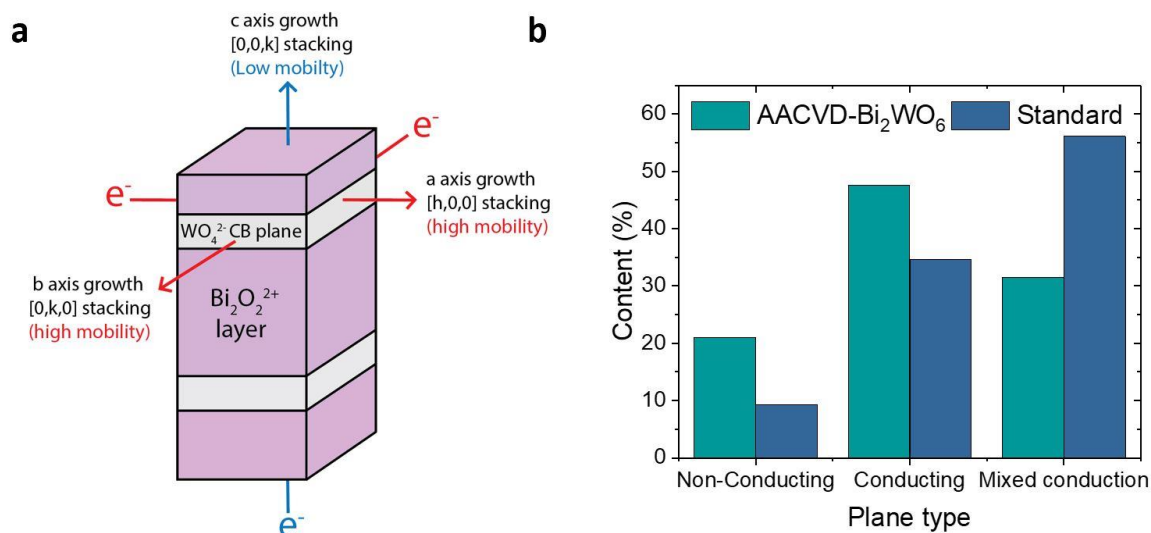
Figure 4 (a) schematic of the layered orthorhombic unit cell of Bi_2WO_6 illustrating the connection between electron transport and preferred growth arising from a CB limited to planes in the material. (b) Quantification of the growth planes of the material, in comparison to a single crystal standard categorised according to the directions of growth shown in (a). Mixed mobility planes are planes which grow the crystal in both favourable and unfavourable direction simultaneously.

directions would occur simultaneously ('mixed mobility' (0,k,l), (h,0,l) and (h,k,l) planes). From this analysis, it is apparent that the crystallites that make up the AACVD Bi_2WO_6 film grow more in directions that are favourable to electron transport in comparison to the crystallographic standard (47% *vs* 36%), at the expense of mixed favourability planes (31% *vs* 56%). However, a significant and increased fraction of unfavourable growth is also observed (21% vs 9.2%). The predominance of low and mixed growth directions, combined with the presumably random orientation of the crystallites with respect to one another, may account for the extremely slow electron transport observed within the films.

Conclusion

In summary, Bi_2WO_6 photoanodes were synthesised by AACVD. The coatings possessed a rough topography formed of micron-sized mounds made up of smaller crystallites. Our photoanodes show relatively early onset potentials for photoelectrochemical water oxidation, but low photocurrents in comparison to other better studied metal oxides. With the exception of TiO_2, ultra-fast recombination in Bi_2WO_6 was slightly slower than other oxides, whilst water oxidation rate constants were similar to other metal oxides (excepting WO_3). However, electron extraction in Bi_2WO_6 is 10-100 times slower than in these materials. Analysis of the band structure of Bi_2WO_6 obtained from DFT shows that the layered structure of Bi_2WO_6 leads to confinement of the CB to $(WO_4^{2-})_n$ planes running through the material. This localisation produces slow electron transport in the direction perpendicular to the CB plane. This concept leads to a clear design principle for Bi_2WO_6, as strong preferred or epitaxial growth along conduction band planes should lead to improved performance. Anisotropic electron transport should, in principle, arise in any layered metal oxide in which the metals are segregated into separate 2d planes, these results are likely to be of great significance to a wide range of upcoming oxide materials for numerous catalytic processes. We therefore suggest preferred or epitaxial growth along CB planes as a general strategy to overcome poor electron transport in such layered oxides.

Supplementary information

The Supporting Information is available free of charge at

The SI contains: XPS, SEM/EDX, Ground state reflectance spectra, PEC stability under intense UV irradiation, TA kinetics, Fitting of TA kinetics, XRD fitting.

Author contributions

B.M. wrote the research article and carried out PEC, SEM, EDX and XPS measurements. C.S.-V. carried out HR-TEM measurements. H.L. and Y.C. synthesised the Bi_2WO_6 photoanodes, carried out physical characterisations and measured their photoelectrochemical performance. A.B. carried out photoelectrochemical measurements and conducted a literature review on Bi_2WO_6 photoanodes and photocatalysts. S.C. conducted ultra-fast TAS studies. K.M performed DFT calculations. S.S provided ultra-fast TAS data for comparison. A.W. conducted photoelectrochemical measurements. C.B. oversaw and provided access to CVD facilities to carry out this work. J.R.D. oversaw and provided access to TAS facilities. A.W oversaw and provided access to DFT facilities. A.K. directed the research, helped to draft the manuscript and carried out slow-timescale TAS measurements. All authors contributed to the analysis and editing of the manuscript.

References
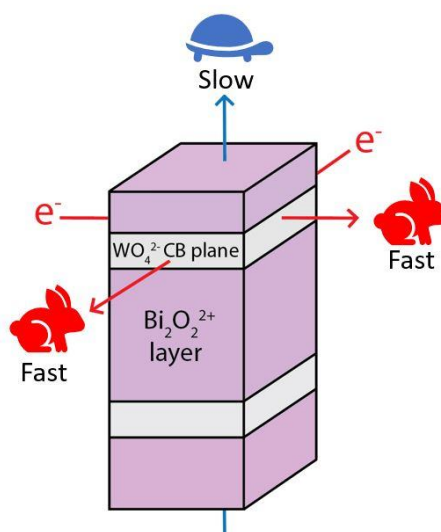
(1)   Broecker, W. S. Climatic Change: Are We on the Brink of a Pronounced Global Warming? *Science (80-.).* **1975**, *189* (4201), 460–463.

(2)   Gruber, N. Warming up, Turning Sour, Losing Breath: Ocean Biogeochemistry under Global Change. *Philos. Trans. A. Math. Phys. Eng. Sci.* **2011**, *369* (1943), 1980–1996.

(3)   Staffell, I.; Scamman, D.; Abad, A. V.; Balcombe, P.; Dodds, P. E.; Ekins, P.; Shah, N.; Ward, K. R. The Role of Hydrogen and Fuel Cells in the Global Energy System. *Energy Environ. Sci.* **2019**, *12* (2), 463–491.

(4)   Brandon, N. P.; Kurban, Z. Clean Energy and the Hydrogen Economy. *Philos. Trans. R. Soc. A Math. Phys. Eng. Sci.* **2017**, *375* (2098), 20160400.

(5)   Sivula, K. Toward Economically Feasible Direct Solar-to-Fuel Energy Conversion. *Journal of Physical Chemistry Letters*. 2015, pp 975–976.

(6)   Shaner, M. R.; Atwater, H. A.; Lewis, N. S.; McFarland, E. W. A Comparative Technoeconomic Analysis of Renewable Hydrogen Production Using Solar Energy. *Energy Environ. Sci.* **2016**, *9* (7), 2354–2371.

(7)   Rothschild, A.; Dotan, H. Beating the Efficiency of Photovoltaics-Powered Electrolysis with Tandem Cell Photoelectrolysis. *ACS Energy Lett.* **2017**, *2* (1), 45–51.

(8)   Yang, Y.; Niu, S.; Han, D.; Liu, T.; Wang, G.; Li, Y. Progress in Developing Metal Oxide Nanomaterials for Photoelectrochemical Water Splitting. *Adv. Energy Mater.* **2017**, *7* (19), 1700555.

(9)   Sivula, K.; Van De Krol, R. Semiconducting Materials for Photoelectrochemical Energy Conversion. *Nat. Rev. Mater.* **2016**, *1* (2), 15010.

(10)   Lee, D. K.; Lee, D.; Lumley, M. A.; Choi, K. S. Progress on Ternary Oxide-Based Photoanodes for Use in Photoelectrochemical Cells for Solar Water Splitting. *Chemical Society Reviews*. Royal Society of Chemistry 2019, pp 2126–2157.

(11)   Zhang, N.; Ciriminna, R.; Pagliaro, M.; Xu, Y. J. Nanochemistry-Derived Bi2WO6 Nanostructures: Towards Production of Sustainable Chemicals and Fuels Induced by Visible Light. *Chem. Soc. Rev.* **2014**, *43* (15), 5276–5287.

(12)   Kendall, K. R.; Navas, C.; Thomas, J. K.; Zur Loye, H. C. Recent Developments in Oxide Ion Conductors: Aurivillius Phases. *Chem. Mater.* **1996**, *8* (3), 642–649.

(13)   Morita, K.; Park, J. S.; Kim, S.; Yasuoka, K.; Walsh, A. Crystal Engineering of Bi2WO6 to Polar Aurivillius-Phase Oxyhalides. *J. Phys. Chem. C* **2019**, *123* (48), 29155–29161.

(14)   Kunioku, H.; Higashi, M.; Tomita, O.; Yabuuchi, M.; Kato, D.; Fujito, H.; Kageyama, H.; Abe, R. Strong Hybridization between Bi-6s and O-2p Orbitals in Sillén-Aurivillius Perovskite Bi4MO8X (M = Nb, Ta; X = Cl, Br), Visible Light Photocatalysts Enabling Stable Water Oxidation. *J. Mater. Chem. A* **2018**, *6* (7), 3100–3107.

(15)   Jiang, B.; Zhang, P.; Zhang, Y.; Wu, L.; Li, H.; Zhang, D.; Li, G. Self-Assembled 3D Architectures of Bi 2TiO 4F 2 as a New Durable Visible-Light Photocatalyst. *Nanoscale* **2012**, *4* (2), 455–460.

(16)   Sun, S.; Wang, W.; Jiang, D.; Zhang, L.; Li, X.; Zheng, Y.; An, Q. Bi2WO6 Quantum Dot-Intercalated Ultrathin Montmorillonite Nanostructure and Its Enhanced Photocatalytic Performance. *Nano Res.* **2014**, *7* (10), 1497–1506.

(17)   Zhang, L.; Zhu, Y. A Review of Controllable Synthesis and Enhancement of Performances of Bismuth Tungstate Visible-Light-Driven Photocatalysts. *Catal. Sci. Technol.* **2012**, *2* (4), 694–706.

(18)   Huang, H.; Liu, K.; Chen, K.; Zhang, Y.; Zhang, Y.; Wang, S. Ce and F Comodification on the Crystal Structure and Enhanced Photocatalytic Activity of Bi 2 WO 6 Photocatalyst under Visible Light Irradiation. *J. Phys. Chem. C* **2014**, *118* (26), 14379–14387.

(19)   Chae, S. Y.; Lee, E. S.; Jung, H.; Hwang, Y. J.; Joo, O. S. Synthesis of Bi2WO6 Photoanode on Transparent Conducting Oxide Substrate with Low Onset Potential for Solar Water Splitting. *RSC Adv.* **2014**, *4* (46), 24032–24037.

(20)   Jian, J.; Jiang, G.; van de Krol, R.; Wei, B.; Wang, H. Recent Advances in Rational Engineering of Multinary Semiconductors for Photoelectrochemical Hydrogen Generation. *Nano Energy* **2018**, *51*, 457–480.

(21)   Kudo, A.; Hijii, S. H2 or O2 Evolution from Aqueous Solutions on Layered Oxide Photocatalysts Consisting of Bi3+ with 6s2 Configuration and D0 Transition Metal Ions. *Chem. Lett.* **1999**, *28* (10), 1103–1104.

(22)   Dumrongrojthanath, P.; Thongtem, T.; Phuruangrat, A.; Thongtem, S. Synthesis and Characterization of Hierarchical Multilayered Flower-like Assemblies of Ag Doped Bi2WO6 and Their Photocatalytic Activities. *Superlattices Microstruct.* **2013**, *64*, 196–203.

(23)   Zhang, L.; Bahnemann, D. Synthesis of Nanovoid Bi2WO6 2D Ordered Arrays as Photoanodes

for Photoelectrochemical Water Splitting. *ChemSusChem* **2013**, *6* (2), 283–290.

(24) Zhang, L.; Baumanis, C.; Robben, L.; Kandiel, T.; Bahnemann, D. Bi 2WO 6 Inverse Opals: Facile Fabrication and Efficient Visible-Light-Driven Photocatalytic and Photoelectrochemical Water-Splitting Activity. *Small* **2011**, *7* (19), 2714–2720.

(25) Hill, J. C.; Choi, K. S. Synthesis and Characterization of High Surface Area CuWO4 and Bi2WO6 Electrodes for Use as Photoanodes for Solar Water Oxidation. *J. Mater. Chem. A* **2013**, *1* (16), 5006–5014.

(26) Dong, G.; Zhang, Y.; Bi, Y. The Synergistic Effect of Bi 2 WO 6 Nanoplates and Co 3 O 4 Cocatalysts for Enhanced Photoelectrochemical Properties. *J. Mater. Chem. A* **2017**, *5* (39), 20594–20597.

(27) Dong, G.; Zhang, Y.; Wang, W.; Wang, L.; Bi, Y. Facile Fabrication of Nanoporous Bi 2 WO 6 Photoanodes for Efficient Solar Water Splitting. *Energy Technol.* **2017**, *5* (11), 1912–1918.

(28) Dong, G.; Hu, H.; Wang, L.; Zhang, Y.; Bi, Y. Remarkable Enhancement on Photoelectrochemical Water Splitting Derived from Well-Crystallized Bi 2 WO 6 and Co(OH) x with Tunable Oxidation State. *J. Catal.* **2018**, *366*, 258–265.

(29) Song, X. C.; Zheng, Y. F.; Ma, R.; Zhang, Y. Y.; Yin, H. Y. Photocatalytic Activities of Mo-Doped Bi 2WO 6 Three-Dimensional Hierarchical Microspheres. *J. Hazard. Mater.* **2011**, *192* (1), 186–191.

(30) Li, Y.; Liu, J.; Huang, X.; Yu, J. Carbon-Modified Bi2WO6 Nanostructures with Improved Photocatalytic Activity under Visible Light. *Dalt. Trans.* **2010**, *39* (14), 3420–3425.

(31) Fu, Y.; Chang, C.; Chen, P.; Chu, X.; Zhu, L. Enhanced Photocatalytic Performance of Boron Doped Bi2WO6 Nanosheets under Simulated Solar Light Irradiation. *J. Hazard. Mater.* **2013**, *254–255* (1), 185–192.

(32) Zhong, Y.; He, Z.; Chen, D.; Hao, D.; Hao, W. Enhancement of Photocatalytic Activity of Bi 2 MoO 6 by Fluorine Substitution. *Appl. Surf. Sci.* **2019**, *467–468*, 740–748.

(33) Zhang, Z.; Wang, W.; Gao, E.; Shang, M.; Xu, J. Enhanced Photocatalytic Activity of Bi 2WO 6 with Oxygen Vacancies by Zirconium Doping. *J. Hazard. Mater.* **2011**, *196*, 255–262.

(34) Hu, J.; Chen, D.; Mo, Z.; Li, N.; Xu, Q.; Li, H.; He, J.; Xu, H.; Lu, J. Z-Scheme 2D/2D Heterojunction of Black Phosphorus/Monolayer Bi 2 WO 6 Nanosheets with Enhanced Photocatalytic Activities. *Angew. Chemie - Int. Ed.* **2019**, *58* (7), 2073–2077.

(35) Zhao, J.; Yang, Y.; Dong, X.; Ma, Q.; Yu, W.; Wang, J.; Liu, G. Electrospinning Construction of Bi2WO6/RGO Composite Nanofibers with Significantly Enhanced Photocatalytic Water Splitting Activity. *RSC Adv.* **2016**, *6* (69), 64741–64748.

(36) Rauf, A.; Ma, M.; Kim, S.; Shah, M. S. A. S.; Chung, C. H.; Park, J. H.; Yoo, P. J. Mediator- and Co-Catalyst-Free Direct Z-Scheme Composites of Bi2WO6-Cu3P for Solar-Water Splitting. *Nanoscale* **2018**, *10* (6), 3026–3036..

(37) Joshi, B.; Yoon, H.; Kim, H.; Kim, M. W.; Mali, M. G.; Al-Deyab, S. S.; Yoon, S. S. Heterojunction Photoanodes for Solar Water Splitting Using Chemical-Bath-Deposited In2O3 Micro-Cubes and Electro-Sprayed Bi2WO6 Textured Nanopillars. *RSC Adv.* **2015**, *5* (104), 85323–85328.

(38) Hao, H.; Lu, D.; Wang, Q. Photoelectrochemical Study on Charge Separation Mechanisms of Bi2WO6 Quantum Dots Decorated G-C3N4. *Int. J. Hydrogen Energy* **2018**, *43* (18), 8824–8834.

(39) Godin, R.; Kafizas, A.; Durrant, J. R. Electron Transfer Dynamics in Fuel Producing Photosystems.

Current Opinion in Electrochemistry. 2017, pp 136–143.

(40) Zhang, G.; Hu, Z.; Sun, M.; Liu, Y.; Liu, L.; Liu, H.; Huang, C. P.; Qu, J.; Li, J. Formation of Bi2WO6 Bipyramids with Vacancy Pairs for Enhanced Solar-Driven Photoactivity. *Adv. Funct. Mater.* **2015**, *25* (24), 3726–3734..

(41) Saison, T.; Gras, P.; Chemin, N.; Chanéac, C.; Durupthy, O.; Brezová, V.; Colbeau-Justin, C.; Jolivet, J. P. New Insights into Bi2WO6 Properties as a Visible-Light Photocatalyst. *J. Phys. Chem. C* **2013**, *117* (44), 22656–22666.

(42) Zhang, G.; Cao, J.; Huang, G.; Li, J.; Li, D.; Yao, W.; Zeng, T. Facile Fabrication of Well-Polarized Bi 2 WO 6 Nanosheets with Enhanced Visible-Light Photocatalytic Activity. *Catal. Sci. Technol.* **2018**, *8* (24), 6420–6428.

(43) Zhou, Y.; Zhang, X.; Zhang, Q.; Dong, F.; Wang, F.; Xiong, Z. Role of Graphene on the Band Structure and Interfacial Interaction of Bi2WO6/Graphene Composites with Enhanced Photocatalytic Oxidation of NO. *J. Mater. Chem. A* **2014**, *2* (39), 16623–16631.

(44) Xie, T.; Liu, Y.; Wang, H.; Wu, Z. Synthesis of α-Fe 2 O 3 /Bi 2 WO 6 Layered Heterojunctions by in Situ Growth Strategy with Enhanced Visible-Light Photocatalytic Activity. *Sci. Rep.* **2019**, *9* (1), 1–12.

(45) Corby, S.; Francàs, L.; Selim, S.; Sachs, M.; Blackman, C.; Kafizas, A.; Durrant, J. R. Water Oxidation and Electron Extraction Kinetics in Nanostructured Tungsten Trioxide Photoanodes. *J. Am. Chem. Soc.* **2018**, *140* (47), 16168–16177.

(46) Physical Sciences Data science Service. https://icsd.psds.ac.uk/

(47) RRUFF database of Raman spectroscopy, X-ray diffraction and chemistry of minerals. https://rruff.info/

(48) Casa Software Ltd. http://www.casaxps.com/

(49) Blöchl, P. E. Projector Augmented-Wave Method. *Phys. Rev. B* **1994**, *50* (24), 17953–17979.

(50) Kresse, G.; Furthmüller, J. Efficient Iterative Schemes for Ab Initio Total-Energy Calculations Using a Plane-Wave Basis Set. *Phys. Rev. B - Condens. Matter Mater. Phys.* **1996**, *54* (16), 11169–11186.

(51) Kresse, G.; Furthmüller, J. Efficiency of Ab-Initio Total Energy Calculations for Metals and Semiconductors Using a Plane-Wave Basis Set. *Comput. Mater. Sci.* **1996**, *6* (1), 15–50.

(52) Momma, K.; Izumi, F. VESTA 3 for Three-Dimensional Visualization of Crystal, Volumetric and Morphology Data. *J. Appl. Crystallogr.* **2011**, *44* (6), 1272–1276.

(53) Kafizas, A.; Francàs, L.; Sotelo-Vazquez, C.; Ling, M.; Li, Y.; Glover, E.; McCafferty, L.; Blackman, C. S.; Darr, J. A.; Parkin, I. P. Optimizing The Activity of Nano-Needle Structured WO3 Photoanodes for Solar Water Splitting – Direct Synthesis Via Chemical Vapor Deposition. *J. Phys. Chem. C* **2017**, *121* (11), 5983–5993.

(54) Rae, A. D.; Thompson, J. G.; Withers, R. L. Structure Refinement of Commensurately Modulated Bismuth Tungstate, Bi2WO6. *Acta Crystallogr. Sect. B Struct. Sci.* **1991**, *47* (6), 870–881.

(55) Yashima, M.; Ishimura, D. Crystal Structure and Disorder of the Fast Oxide-Ion Conductor Cubic Bi2O3. *Chem. Phys. Lett.* **2003**, *378* (3–4), 395–399.

(56) Pendlebury, S. R.; Wang, X.; Le Formal, F.; Cornuz, M.; Kafizas, A.; Tilley, S. D.; Grätzel, M.; Durrant, J. R. Ultrafast Charge Carrier Recombination and Trapping in Hematite Photoanodes

under Applied Bias. *J. Am. Chem. Soc.* **2014**, *136* (28), 9854–9857.

(57) Moss, B.; Lim, K. K.; Beltram, A.; Moniz, S.; Tang, J.; Fornasiero, P.; Barnes, P.; Durrant, J.; Kafizas, A. Comparing Photoelectrochemical Water Oxidation, Recombination Kinetics and Charge Trapping in the Three Polymorphs of TiO2. *Sci. Rep.* **2017**, *7* (1), 2938.

(58) Sachs, M.; Pastor, E.; Kafizas, A.; Durrant, J. R. Evaluation of Surface State Mediated Charge Recombination in Anatase and Rutile TiO2. *J. Phys. Chem. Lett.* **2016**, *7* (19), 3742–3746..

(59) Selim, S.; Pastor, E.; García-Tecedor, M.; Morris, M. R.; Franca, L.; Sachs, M.; Moss, B.; Corby, S.; Mesa, C. A.; Gimenez, S.; Kafizas, A.; Bakulin, A. A.; Durrant, J. R. Impact of Oxygen Vacancy Occupancy on Charge Carrier Dynamics in BiVO 4 Photoanodes. *J. Am. Chem. Soc* **2019**, *16*, 12.

(60) Nelson, J.; Chandler, R. E. Random Walk Models of Charge Transfer and Transport in Dye Sensitized Systems. *Coord. Chem. Rev.* **2004**, *248* (13–14), 1181–1194.

(61) Ma, Y.; Pendlebury, S. R.; Reynal, A.; Le Formal, F.; Durrant, J. R. Dynamics of Photogenerated Holes in Undoped BiVO4 Photoanodes for Solar Water Oxidation. *Chem. Sci.* **2014**, *5* (8), 2964–

(62) Zachäus, C.; Abdi, F. F.; Peter, L. M.; Van De Krol, R. Photocurrent of BiVO4 Is Limited by Surface Recombination, Not Surface Catalysis. *Chem. Sci.* **2017**, *8* (5), 3712–3719.

(63) Kafizas, A.; Ma, Y.; Pastor, E.; Pendlebury, S. R.; Mesa, C.; Francas, L.; Le Formal, F.; Noor, N.; Ling, M.; Sotelo-Vazquez, C.; Carmalt, C. J.; Parkin, I. P.; Durrant, J. R. Water Oxidation Kinetics of Accumulated Holes on the Surface of a TiO2 Photoanode: A Rate Law Analysis. *ACS Catal.* **2017**, *7*, 4896–4903.

(64) Formal, F. Le; Pendlebury, S. R.; Cornuz, M.; Tilley, S. D.; Graetzel, M.; Durrant, J. R. Back Electron – Hole Recombination in Hematite Photoanodes for Water Splitting. *J. Am. Chem. Soc.* **2014**, *136*, 2564–2574.

(65) Walsh, A.; Yan, Y.; Huda, M. N.; Al-Jassim, M. M.; Wei, S. H. Band Edge Electronic Structure of BiVO 4: Elucidating the Role of the Bi s and V d Orbitals. *Chem. Mater.* **2009**, *21* (3), 547–551.

TOC graphic